Optimized Reduction in Draft Tube Pressure Pulsation for a Francis Turbine

J. Lu[1] and R. Tao[1, 2, †]

[1] College of Water Resources and Civil Engineering, China Agricultural University, Beijing 100083, China
[2] Beijing Engineering Research Center of Safety and Energy Saving Technology for Water Supply Network System, Beijing 100083, China

[†] Corresponding Author Email: randytao@cau.edu.cn

ABSTRACT

As a core component of hydroelectric power generation, the stable and safe operation of the Francis turbine is very important for the operation of the project. Therefore, attention must be paid to the problem of pressure pulsation in the Francis turbine. In this study, the efficiency, power, and pressure pulsation of the turbine are first compared based on computational fluid dynamics (CFD), combined with numerical simulation and experimental results. It was found that the numerical simulation method was reliable. Therefore, based on the genetic algorithm (GA) and pulsation tracking network (PTN), this article optimizes the draft tube pressure pulsation (DTPP) problem of the Francis turbine and finds that the DTPP is mainly dominated by rotation frequencies (fn) of 0.2, 0.4, 0.6, and 0.8. This research optimized the placement angle of the runner blade's 0.75span and 1.0span using the genetic algorithm. The PTN method was used to analyze the changes in pressure pulsation signals from the perspectives of the pressure velocity vector, main frequency, pulsation intensity, and phase change. After optimization, the value of $\beta 0.75$ was reduced from 160.59° to 160.452°, and the value of $\beta 1.0$ was increased from 160.6° to 161.865°. The pressure pulsation intensity of each working condition was also weakened. Therefore, this research provides a new and effective analysis and optimization method for the pressure pulsation problem in turbine machinery.

1. INTRODUCTION

Due to the excessive exploitation and use of fossil energy, carbon dioxide emissions have increased and the ecological environment is deteriorating (Kekes 2011; Mayer, 2022). Therefore, the energy consumption structure has started to be reformed. In the current energy structure, renewable energies such as wind energy, tidal energy, and solar energy are already being applied in various fields. Therefore, more attention is being paid to the development of cleaner, more sustainable and efficient hydropower energy (Zhang et al., 2022; Nasir et al., 2022). The Francis turbine is a core component of hydropower generation that converts the potential energy of water into electric energy. However, due to the extra tangential momentum in the outlet angle of the runner blade of the Francis turbine, the water flows out of the runner into the draft tube with circumferential velocity (Yang et al., 2022). In this case, a vortex rope may be formed in the draft tube, resulting in strong pressure pulsation, causing vibrations in the turbine unit, accompanied by huge noise,

which will affect the operating life of the turbine unit and even cause engineering accidents (Wang et al., 2021). Therefore, the stability of the draft tube in the running process of the Francis turbine is a concern of many researchers.

As an important component of the Francis turbine, the performance of the draft tube can directly affect the operating efficiency and stability of the turbine unit to a certain extent (Amooghin et al., 2015; Joy et al.2022). The flow characteristics of the water in the draft tube can be changed according to the operating conditions, such as adjusting the opening of the guide vane of a Francis turbine or adjusting the blade angle of an axial flow slurry turbine. Both changes will affect the draft tube flow field (Wang et al., 2018; Chen et al., 2019). Many notable researchers have conducted in-depth analyses on how to weaken the pressure pulsation caused by the vortex rope of the draft tube, mainly using geometric methods and fluid methods (Kumar et al., 2021). Luo et al. (2022) studied the influence of a J-shaped groove on eddy current suppression and energy dissipation of the diversion tube

using numerical simulation. The entropy production theory was used to calculate the loss of energy coherence. The results show that the J-shaped groove has a good inhibition effect on eddy current control and energy dissipation of the draft tube of the Francis turbine. Zhou et al. (2021) proposed a new method for reducing vortex ropes, which uses an improved draft tube with an inclined cone diffuser. The CFD calculation results show that an inclination of 8.2021 degrees is the most effective way to hinder the development of strong turbulent flow and thus reduce the amplitude of pressure pulsation. The experimental study published by Bosioc et al. (2012) designed a method for the pressure pulsation measurement of the cone draft tube wall. The Fourier transform of the pressure fluctuations was analyzed to assess how water injection changes the amplitude and dominant frequency. The results show that the water jet injection significantly reduces the amplitude and frequency of pressure pulsation and improves the pressure recovery ability of the conical draft tube. Chirkov et al. (2018) studied the flow mixing of liquid and steam as a three-dimensional model by studying the air injection under the runner during turbine operation and described the boundary conditions and numerical methods used to solve the model equations. Their results show that with the increase in airflow, the amplitude of the pressure pulsation decreases, which explains the mechanism of flow structure change in the cone of the diversion tube, resulting in stable flow during air injection. Abu Shahzer et al. (2023) observed that the cavitation vortex rope under partial load leads to severe pressure fluctuations and reductions in the Francis turbine's efficiency at a low cavitation number and conducted numerical simulation of the flow characteristics of turbines with and without fins in the draft tube. The results show that installing fins on the draft tube can improve the stability of the unit to the greatest extent. These methods can effectively reduce the DTPP. However, these methods are not suitable for turbines where the draft tube cannot be changed. Therefore, in order to improve the operation efficiency and stability of the Francis turbine unit, it is of great engineering significance to carry out comprehensive design optimization for the runner (Yu et al., 2019; Li et al., 2021a, b; Kan et al., 2023a,b).

The formation principle of the vortex rope in the draft tube was mentioned earlier. According to an analysis based on the velocity triangle at the runner blade outlet, if the water flows out from the runner blade outlet and normally flows into the draft tube inlet, there will be no vortex rope and the pressure pulsation will disappear (Wang et al., 2002; Zheng et al., 2018; Yu et al., 2021). However, it is difficult to achieve the normal flow of water into the draft tube in practical engineering. Therefore, this research carries out optimization design for the runner and finds that the optimization strategy of the genetic algorithm (GA) has great advantages (Ge et al., 2008; Tao et al., 2014, 2018; Lu et al., 2023). For example, Sato et al. (2014) developed a multi-objective optimization system for Francis turbine runners using the genetic algorithm. Their research goal was to develop an automatic design system for Francis turbine runners and evaluate its usability. The results show that the optimized

flow passage using the baseline design can be obtained efficiently and automatically through an iterative design program. Moreover, Miao et al. (2015) proposed a multi-conditional optimization approach based on a neural network and genetic algorithm for the blade pattern of the hydraulic turbine, based on which the blade profile was optimized and improved. Sato et al. (2014) developed a multi-objective optimization system for Francis turbine runners using the genetic algorithm and evaluated its usability. Furthermore, the pulsation tracking network (PTN) can be used to visualize and trace pressure pulsation signals (Jin et al., 2021; Lu et al., 2021). In this method, the fast Fourier transform (FFT) of the pressure pulsation signal (Graham et al., 2016) is decomposed, and its frequency, amplitude, and phase are visually analyzed to provide a reference direction for optimization design .

This article presents a deep analysis and tracing of the pressure pulsation problem in Francis turbines, aiming to establish an optimized parameter model of the matching relationship between the runner and draft tube. The PTN method combined with GA is employed, with the runner blade outlet angle taken as the optimization objective and the turbine efficiency and pressure pulsation used as the evaluation criteria. The results indicate that the proposed optimization strategy is not only feasible but also effective. This provides certain reference value for mitigating pressure pulsation issues and improving the efficiency of hydropower turbine units in engineering applications.

2. RESEARCH OBJECTIVE

The objective of this study is to investigate the Francis turbine, as depicted in Fig. 1. The fluid domain consists of the volute, stay vanes, guide vanes, runner, and draft tube. The fluid flows out from the volute outlet, then passes through the stay and guide vanes, and flows out from the runner, entering the draft tube. In the initial model of the Francis turbine, the runner is the only rotating component of the entire turbine, operating at a rated speed of 1450 r/min. Table 1 presents the relevant geometric parameters of the turbine. The aim of this study is to enhance the operational efficiency of the turbine while reducing the pressure pulsation in the draft tube. The efficiency (η) and DTPP intensity (C_p) are important parameters that signify the performance of the turbine, with efficiency represented by Eq. (1).

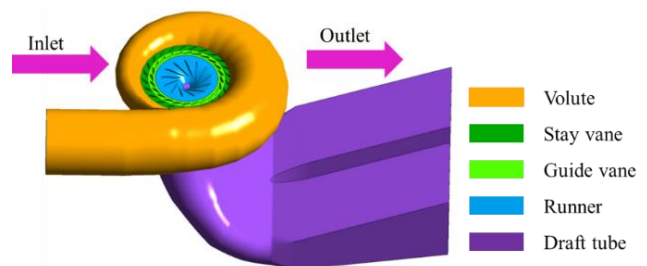**Fig. 1 Three-dimensional model of objective Francis turbine**

Table 1 Geometric parameters of objective Francis turbine

Parameters	Value	Unit
Diameter of runner D_M	300	[mm]
Rated rotation speed n_M	1450	[r/min]
Rate head H_M	38.250	[m]
Rated flow rate Q_M	0.604	[m³/s]
Rate power P_M	0.210	[MW]
Guide vane angle α_{ref}	12	[°]
Runner rotation frequency f_n	1.667	[Hz]
Number of stay vanes Z_{svM}	24	[-]
Number of guide vanes Z_{gvM}	24	[-]
Number of runner blades Z_{ruM}	13	[-]

$$\eta = \frac{M\omega}{\rho g Q H} \tag{1}$$

where M is the torque, ω is the angular velocity, ρ is the fluid density, g is the gravitational acceleration, Q is the flow rate, and H is the head.

This research defines the dimensionless parameter for DTPP intensity C_p using Eq. (2).

$$C_p = \frac{\Delta p}{\rho g H} \tag{2}$$

where Δp is the peak-to-peak pressure pulsation.

3. METHODOLOGY

3.1 Experimental Method

3.1.1 Test Rig and Facilities

In order to demonstrate the reliability of numerical simulations and enhance the credibility of our numerical simulations, this study adopts a combined approach of

practical experiments and numerical simulations. The overall structure of the closed hydraulic experimental setup is shown in Fig. 2, which mainly consists of a fluid transportation system and an information collection system.

The fluid transportation system includes a Francis turbine, upstream and downstream water tanks, an electric

motor, a supply pump, pipelines, and valves. The information collection system comprises pressure sensors, an electromagnetic flow meter, load sensors and exciters, dynamic pressure pulsation sensors, and PCB signal amplifiers. The pressure sensors are used to measure the upstream and downstream pressure values (P_1 and P_2) of the hydropower turbine. The hydraulic head is calculated based on the pressure difference using Eq. (3), with a measurement error not exceeding ±0.1%. An electromagnetic flow meter is employed to measure the flow rate (Q) inside the pipelines, with an instrument measurement error not exceeding ±2%. Load sensors and exciters are utilized to measure the torque (M) acting on the hydropower turbine shaft, with instrument errors not exceeding ±0.05% and ±0.02%, respectively. The rotational angular velocity (ω) can be measured using a rotational encoder, and therefore, the power (P_z) can be calculated using Eq. (4). The pressure pulsation P_{dt} at the monitoring points is measured using dynamic pressure pulsation sensors and PCB signal amplifiers, with an instrument error not exceeding ±1%. The instrumentation used in the experiments and their inaccuracies are listed in Table 2.
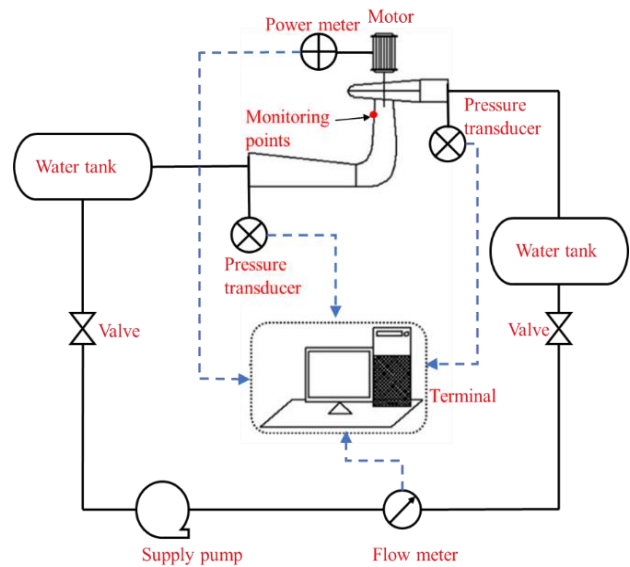

Fig. 2 Experimental flow chart for monitoring the DTPP of Francis turbine

Table 2 Experimental instruments and uncertainty

Quantity	Apparatus	Uncertainty
Pressure of inlet and outlet P_1, P_2	Pressure sensors	±0.1 %
Flow rate Q	Electromagnetic flow meter	±0.2 %
Torque M	Load sensor Excitation amplifier	±0.05 % ±0.02 %
Rotation angular speed ω	Rotary encoder	±0.01°
Draft tube pressure P_{dt}	Dynamic pressure pulsation sensor PCB signal amplifier	±0.1 %

$$H = \frac{P_1 - P_2}{\rho g} \tag{3}$$

$$P_z = M\omega r \tag{4}$$

3.1.2 Test Standard (IEC60193)

The experimental setup used in this study and the relevant measuring instruments meet the accuracy requirements specified in the IEC 60193 standard

(IEC60193., 1999). Since this experiment primarily focuses on monitoring the DTPP, it is important to refer to the IEC 60193 standard for the measurement of pressure pulsations. Due to various interactions with the external environment or differences in fluid characteristics between the model and the actual system, there may be significant differences between the amplitude and frequency of pressure pulsations in the actual system and those obtained from direct model tests. As the deviation between the model and the actual system cannot be determined under current conditions, in most cases, the measurement of model pressure pulsations is conducted to obtain qualitative information or assess the magnitude of pulsations. Furthermore, in order to avoid resonance between the experimental setup and the model, it is important that the natural frequency of the experimental flow does not coincide with the frequency of the model. The hydraulic disturbances caused by the supply pump, valves, and bends should not affect the model setup.

3.2 Numerical Method

3.2.1 Governing Equations

In this study, this research conducted simulation and analysis of a mixed-flow hydropower turbine using computational fluid dynamics (CFD). This research employed Reynolds-Averaged Navier–Stokes (RANS) equations for numerical simulations of a three-dimensional, incompressible fluid. Therefore, the continuity equation, momentum equation, and total energy equation under the RANS method are represented by Eq. (5), Eq. (6), and Eq. (7), respectively.

$$\frac{\partial \overline{u_i}}{\partial x_i} = 0 \tag{5}$$

$$\rho \frac{\partial \overline{u_i}}{\partial t} + \rho \overline{u_j} \frac{\partial \overline{u_i}}{\partial x_j} = \\ \frac{\partial}{\partial x_j}\left(-\overline{p}\delta_{ij} + 2\mu \overline{S_{ij}} - \rho \overline{u_i' u_j'}\right) \tag{6}$$

$$\frac{\partial}{\partial t}(\rho h_{tot}) - \frac{\partial p}{\partial t} + \frac{\partial}{\partial x_j}(\rho u_j h_{tot}) = \\ \frac{\partial}{\partial x_j}\left(\lambda_t \frac{\partial T}{\partial x_j} - \overline{u_j h_{sta}}\right) + \frac{\partial}{\partial x_j}\left[u_j\left(2\mu \overline{S_{ij}} - \rho \overline{u_i' u_j'}\right)\right] \tag{7}$$

where u is the velocity, p is the pressure, t is the time, ρ is the density, T is the temperature, x is the coordinate component, δ_{ij} is the Kroneker delta, μ is the dynamic viscosity, S_{ij} is the mean rate of the strain tensor, h_{sta} is the static enthalpy, h_{tot} is the total enthalpy, and λ_t is the thermal conductivity.

Due to the presence of turbulent fluctuations, it is necessary to close the Navier–Stokes equations using a turbulence model. After comparing different turbulence models, this research found that the SST k-ω turbulence model provides better simulation results for high-Reynolds-number flows and separated flows. It combines the advantages of the k-ω model in the near-wall region and the k-ε model in the far field. Numerous studies have demonstrated that this model is suitable for engineering

problems. Therefore, this research selected the SST k-ω turbulence model, which closes the equations by establishing the relationship between the Reynolds stresses and the eddy viscosity. The turbulent kinetic energy (k) and the dissipation rate transport (ω) are represented by Eq. (8) and Eq. (9), respectively:

$$\frac{\partial(\rho k)}{\partial t} + \frac{\partial(\rho u_i k)}{x_i} = \\ P - \frac{\rho k^{3/2}}{l_{k-w}} + \frac{\partial(\rho k)}{\partial x_i}\left[(\mu + \sigma_k \mu_i)\frac{\partial k}{\partial x_i}\right] \tag{8}$$

$$\frac{\partial(\rho \omega)}{\partial t} + \frac{\partial(\rho u_i \omega)}{x_i} = \\ C_\omega P - \beta \rho \omega^2 + \frac{\partial}{\partial x_i}\left[(\mu_i + \sigma_\omega \mu_i)\frac{\partial \omega}{\partial x_i}\right] + 2(1 - F_1)\frac{\rho \sigma_{\omega 2}}{\omega}\frac{\partial k}{\partial x_i}\frac{\partial \omega}{\partial x_i} \tag{9}$$

where ρ is the fluid density, P is the turbulence generation term, μ is the dynamic viscosity, μ_t is the eddy viscosity coefficient, σ is the model constant, C_ω is the coefficient of turbulent dissipation term, F_1 is the blending equation, and k-ω is the scale of turbulence. In the term $\rho k^{3/2}/l_{k-\omega}$, the expression for the turbulence scale $l_{k-\omega}$ is given by Eq. (10):

$$l_{k-\omega} = k^{1/2}\beta_k \omega \tag{10}$$

3.2.2 Grid Preparation and Check

To perform the numerical simulation, this research employed the finite volume method for grid discretization. In order to ensure computational accuracy while reducing computation time, this research adopted a strategy of using tetrahedral and hexahedral grids for geometric discretization of the model. The runner was meshed using a hexahedral unstructured grid, while the other components were meshed using a tetrahedral structured grid. Considering that the number of grids can also affect the computational results, this research conducted a grid independence study to ensure the rationality of the grid selection for supporting subsequent research. The grid independence study was performed using the Richardson extrapolation method, with the efficiency of the Francis turbine set as the objective function.

This research prepared three sets of grids with different numbers of grid nodes: coarse (N1=7042620), medium (N2=2753686), and fine (N3=1110522). Independent analysis is carried out for the three grid schemes, and details of the independence check results are shown in Fig. 3 (Celik et al., 2008). The refinement factor for medium and coarse grids is 1.354, with a GCI value of 0.0003%; the refinement factor for the fine and medium grids is 1.368, with a GCI value of 0.039%, which satisfies the convergence requirements. The specific details are shown in Table 3. While the three grids all have good convergence, considering the computational accuracy and the computation time, this research ultimately chose the fine grid scheme for the final computation, with a total number of nodes of 1110522. The details of the grid division of the whole fluid domain are shown in Fig. 4 and Table 4.
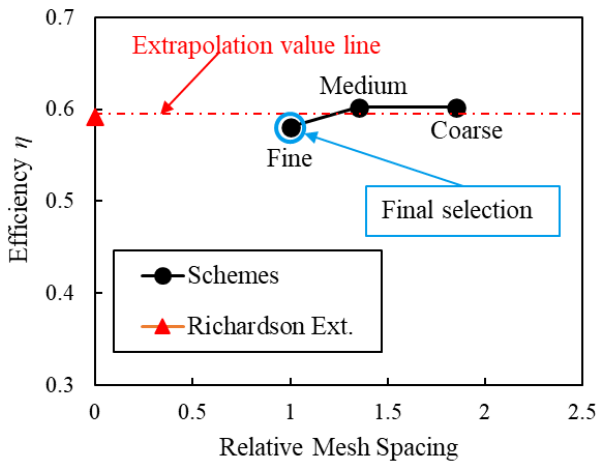
Fig. 3 Details of grid independence test

Table 3 Evaluation results of discretization error

Variation	η
$\Phi 1$	0.580
$\Phi 2$	0.602
$\Phi 3$	0.602
Φ_{ext}^{21}	0.580
e_{ext}^{21}	3.740%
GCI_{fine}^{21}	0.039%
Φ_{ext}^{32}	0.602
e_{ext}^{32}	0.030%
GCI_{fine}^{32}	0.0003%
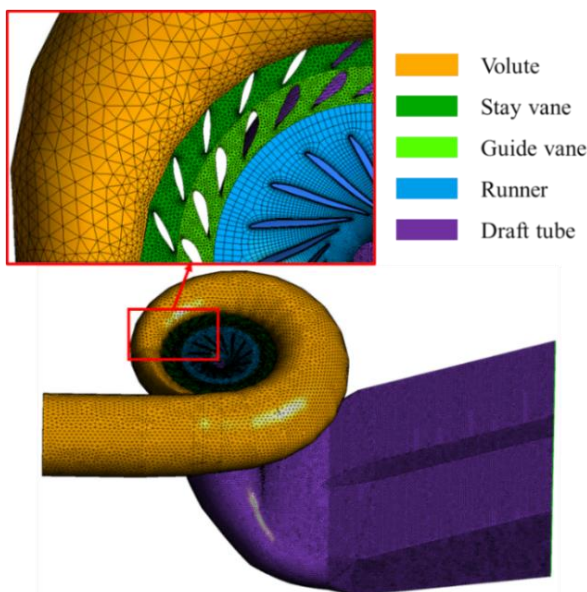
Fig. 4 Grid of objective Francis turbine

Table 4 Type of grid and number of grids for each component of the turbine

Component	Grid element type	Grid element number
Volute	Tetrahedral grid	247915
Stay vane	Tetrahedral grid	1400646
Guide vane	Tetrahedral grid	1604155
Runner	Hexahedral grid	343060
Draft tube	Tetrahedral grid	1348422
Total		4944198

3.2.3 CFD Setup

This study utilizes a turbulence model solver and computational fluid dynamics theory to simulate and analyze a Francis turbine, performed using the commercial software ANSYS CFX. The fluid medium considered is water at a temperature of 25°C. The reference pressure is 1 Atm. In the simulation, the inlet of the volute is set as the inlet of the entire computational domain, with a total pressure inlet boundary condition. The outlet of the draft tube represents the outlet of the entire computational domain and is set as an average static pressure outlet boundary condition. At the outlet, the static pressure is set to 0 Pa, which is equivalent to atmospheric pressure. All wall surfaces are set as no-slip boundaries. A multiple reference frame (MRF) model is used in which the interface between the runner, guide vanes, and the draft tube is set as a dynamic–stationary reference frame, while the rest of the components are set as stationary–stationary reference frames. The general grid interface (GGI) model is employed for data transfer between different components. The SST *k-ω* turbulence model is chosen for modeling the turbulent flow. In the steady-state calculations, the maximum number of iterations is set to 1000, and the results obtained are used as initial conditions for the unsteady calculations. In the unsteady calculations, the rotor is rotated for 10 revolutions, with each step being 2° and iterated 10 times per step. The convergence criterion is set such that the root-mean-square residuals of the continuity equation and momentum equation are less than 1×10^{-5}. The details of the monitoring point placement can be found in Section 3.3.

3.3 Post-Analysis Method

3.3.1 Pulsation Tracking Network (PTN)

Traditional flow field monitoring is often limited by the performance of computers, which typically monitor flow field data at some typical locations and analyze relevant parameters in the time and frequency domains. It is difficult to capture and track the fluctuation signals accurately. Therefore, for the monitoring of fluctuation signals, this research adopted a novel approach known as the pulse tracking network (PTN) method (Jin et al., 2023). This research designed a monitoring point network with high spatial resolution, which consists of monitoring point sequences and three-dimensional spatial coordinate information. Firstly, for the arrangement of monitoring points, they can be divided into a fan-shaped arrangement, rectangular arrangement, circular arrangement, or random arrangement. Constraints should be applied to the distance
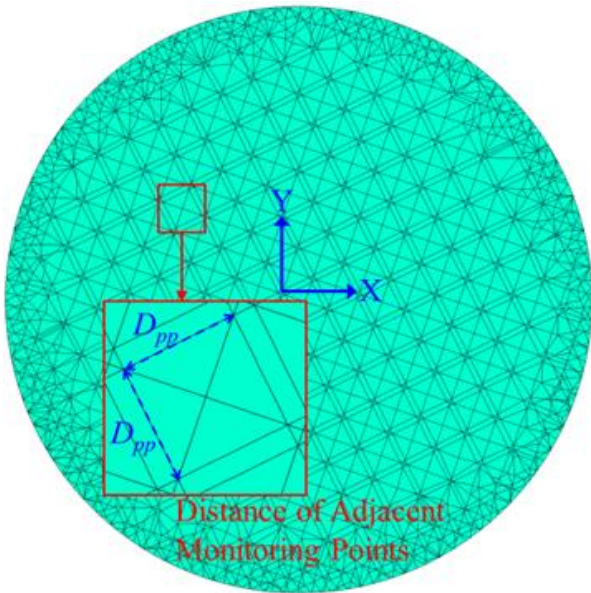
Fig. 5 Distribution of points in the PTN

Fig. 6 Details of the monitoring point layout

Fig. 7 Natural neighbor interpolation from sample points

between monitoring points, and the density of monitoring points should not exceed the number of grid elements to avoid increased computational pressure and obtaining redundant data. Secondly, a reasonable interpolation scheme is required to obtain the results from the CFD grid calculations. Using the PTN method, this research can spatially track the frequency origin of pulsation signals, visualize the pulsation signal intensity, and reveal the phase decay laws of pulsation signals. This study mainly focuses on the analysis of the DTPP, specifically the DTPP issue caused by the geometry of the runner blades.

3.3.2 Setup of PTN

A large number of ordered monitoring points are evenly distributed across two sections, Plane 1 and Plane 2, of the draft tube. This research defined a parameter, D_{pp}, see Eq. (11), which represents the distance between adjacent monitoring points, as shown in Fig. 5.

$$D_{pp} = \frac{C_s v_{ref}}{2\pi f_{ref}} \qquad (11)$$

where v_{ref} is equal to the inlet axial velocity v_{in} of 3.45 m/s, f_{ref} is the runner frequency of about 1.666 Hz, and C_s is the scaling factor for a more uniform distribution of points and for a better resolution. In this study, the initial value of C_s is set to 5~7. Therefore, the value of D_{pp} is approximately 1.65~2.307mm. As a result, 4000 monitoring points are arranged on Plane 1 and 6000 monitoring points are arranged on Plane 2, as shown in Fig. 6. The PTN layout achieves a monitoring point density that matches the CFD grid and provides an optimal spatial resolution.

In this study, the natural neighbor interpolation method was selected based on the random uniform distribution of the monitoring points, as described in Eq. (12):

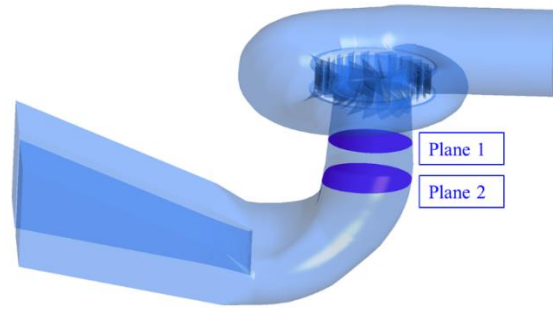$$F(a) = \sum_{i=1}^{n} w_i(a) f_i \qquad (12)$$

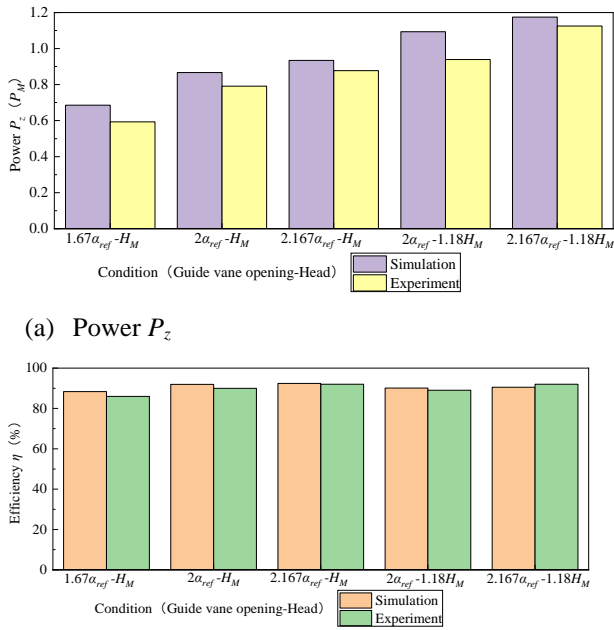where $F(a)$ is the interpolation result at the point to be interpolated (target point), $wi(a)$ is the weight of the interpolation target point of sample point i (i=1, …, n), and f_i is the value at sample point i. For the weight values, this research defined Eq. (13) as follows:

$$W_i(a) = \frac{R_i \cap R(a)}{R(a)} \qquad (13)$$

where R_i is the area of the polygon where the sample points participate in the interpolation, and $R(a)$ is the area of the polygon where the target point is to be interpolated. Therefore, compared to the traditional CFD monitoring point method, the PTN method based on natural neighbor interpolation, as shown in Fig. 7, allows us to obtain data from more grids in the CFD simulation. This provides us with more detailed information for further analysis and interpretation.

4. VALIDATION AND VERIFICATION OF TURBINE PERFORMANCE AND PRESSURE PULSATIONS

Figure 8 shows the comparison between the numerical simulation and experimental results concerning turbine efficiency and power under different guide vane openings and head conditions. Figure 9 shows the relative error changes between the experimental and numerical simulation results, from which it can be seen that, based on the relevant settings of the numerical CFD simulation, the error between the numerical simulation and the experimental results is small and both are in good agreement. The results also show that the numerical

(a) Power P_z

(b) Efficiency η

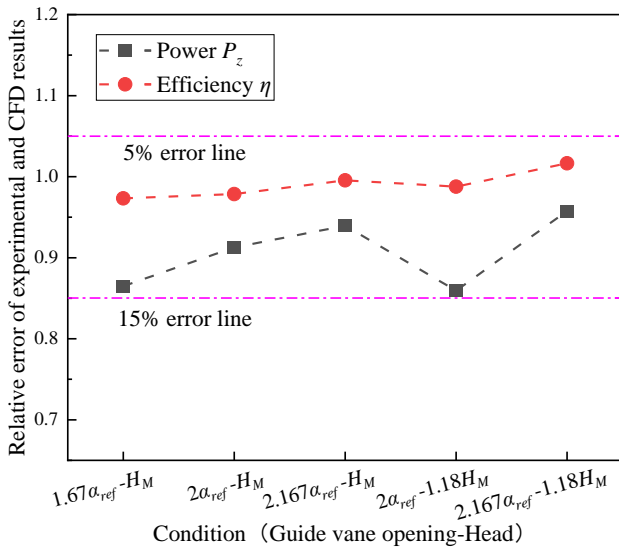**Fig. 8 Comparison of numerical simulation and experimental turbine performance characteristics**

Fig. 9 Comparison of the relative error in the external characteristics of the turbine between the numerical simulation and experiment

Fig. 10 Comparison of pressure pulsation amplitude between experiments and numerical simulation (Condition 1.12 α_{ref}-0.735 H_M)

harmonic frequencies. DTPP is generally a low-frequency pulsation, meaning it more easily resonates with the inherent frequency of the factory building, which is very likely to cause engineering accidents. Therefore, this research aims to reduce the draft tube pressure pulsation as much as possible to ensure or improve the turbine's operating efficiency.

Figure 10 shows the comparison between the experimental pressure pulsations and the numerical simulation results for Condition 1.12 α_{ref}-0.735 H_M. This research performed error analyses on the amplitude of the pressure pulsations in the volute, bladeless region, and draft tube. As can be seen from the figure, the error of the pressure pulsation amplitude in the three regions is within 10%, suggesting that such an error can be used in numerical simulation instead of model tests. Therefore, this research will use the numerical simulation method to optimize the design of the runner outlet blade geometry, to reduce the pressure pulsation in the draft tube, and to improve the operating efficiency of the turbine as much as possible.

5. OPTIMIZATION OF RUNNER

5.1 Parameterization and Coding

The genetic algorithm is used as the optimization algorithm in this study. Parametric control of the runner blade geometry is necessary in order to reduce the pressure pulsations in the draft tube of the Francis turbine and to improve the performance of the unit. The blade placement angle β is shown in Fig. 11 below, which demonstrates the velocity triangle at the outlet of the runner blades, where β is the angle between the relative velocity and the circumferential velocity, also called the relative liquid flow angle. This research focuses on optimizing the blade placement angle for the 0.75span and 1.0span blade heights of the runner (see Fig. 12) and uses the trailing edge angle definition method to control the curve of the blade outlet placement angle (see Fig. 13), optimizing for the trailing edge angle. The initial trailing edge angle $\beta_{0.75}$

simulation method used in this paper has some reliability. From Fig. 8(b), it can be seen that the turbine has higher-efficiency operating conditions, which means that the turbine needs to be frequently operated under high-flow conditions. Therefore, this research needs to pay attention to the stable and safe operation of the turbine, especially considering the pressure pulsation problem. Considering that the strong pressure pulsation region of the Francis turbine generally exists in the bladeless region. The pressure pulsation in the bladeless region mainly takes the form of high-frequency pulsation, which is generally dominated by the runner frequency (octave frequency), blade frequency (octave frequency), or other related
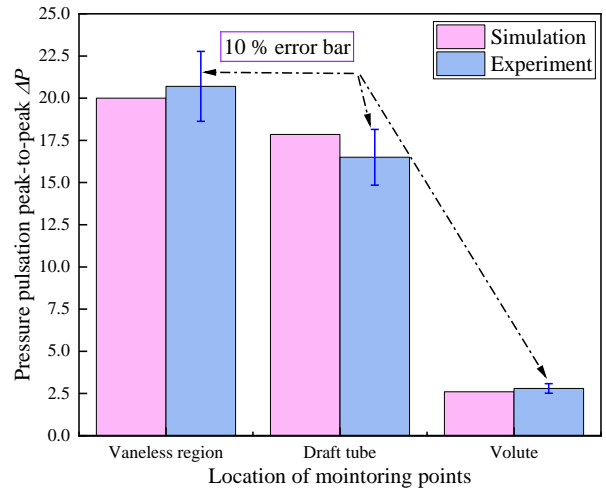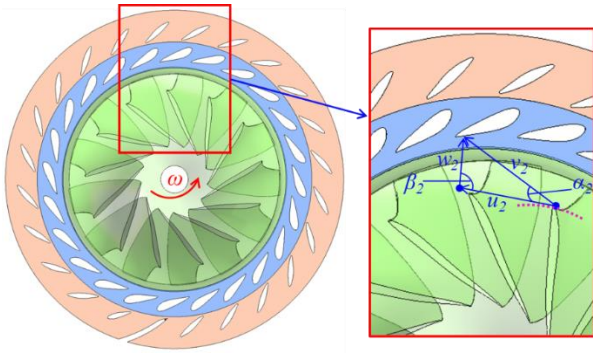
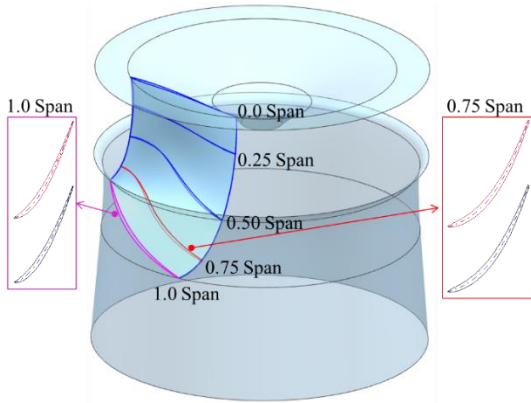**Fig. 11 Diagram of the runner blade outlet velocity triangle**

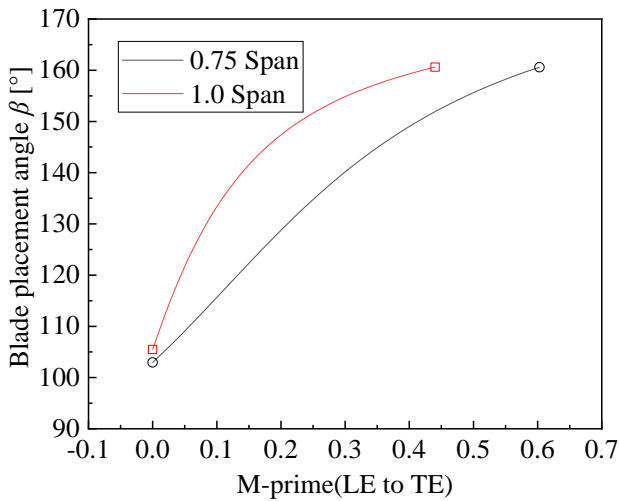**Fig. 12 Diagram of 0.75 span and 1.0 span runner blades**

Fig. 13 Schematic diagram of 0.75 span and 1.0 span runner blade placement angle β control curves

is 160.59°, and $\beta_{1.0}$ is 160.60°. The blade leading edge angle and the blade thickness are both constant.

The control parameters of the blade have been determined before optimizing the target model using the genetic algorithm. To ensure simplicity and clarity for the genetic algorithm, $\beta_{0.75}$ and $\beta_{1.0}$ having been binary coded, and the coding of the two parameters forms an individual value. In this article, a 16-bit binary coding string is used

to describe a parameter. Therefore, a parameter is represented by a 16-bit binary string. $\beta_{0.75}$'s decimal optimization value ranges from 157.746° to 162.746°, and $\beta_{1.0}$'s decimal optimization value ranges from 156.1° to 161.1°, with an accuracy of 0.0196°. Ten individuals are selected as one generation, and a total of ten generations of genetic optimization iterations are carried out to obtain the optimal individual.

5.2 Objective Function

On the basis of effectively controlling the blade profile of the turbine wheel, this research has determined the objective function with efficiency η and pressure fluctuation intensity C_p as optimization objective, the C_p equation is shown in Eq. (2). The weighted control of the optimization objective is achieved by increasing the weighting factors w_1, w_2, x_1, x_2, y_1, and y_2. The objective function Eq. (14) is as follows:

$$G = w_1\left(x_1\eta_1 + x_2\eta_2\right) - $$
$$w_2\left(y_1\left(\frac{C_{p11} + C_{p12}}{2}\right) + y_2\left(\frac{C_{p21} + C_{p22}}{2}\right)\right) \tag{14}$$

where x_1 is the weight factor of the turbine efficiency for condition 2 α_{ref}-H_M, x_1=0.9. η_1 is the turbine efficiency for condition 2 α_{ref}-H_M, x_2 is the weight factor of the turbine efficiency for condition 1.33 α_{ref}-1.18 H_M, x_2=0.1. η_2 is the turbine efficiency for condition 1.33 α_{ref}-1.18 H_M, and y_1 is the weight factor of the turbine pressure fluctuation intensity for condition α_{ref}-H_M, y_1=0.8. Moreover, C_{p11} is the pressure pulsation intensity of Plane 1 for condition α_{ref}-H_M, and C_{p12} is the pressure fluctuation intensity of Plane 2 for condition α_{ref}-H_M. y_2 is the weight factor of the turbine pressure pulsation for condition 1.33 α_{ref}-1.18 H_M, y_2=0.2. C_{p21} is the pressure pulsation intensity of Plane 1 for condition 1.33 α_{ref}-1.18 H_M, and C_{p22} is the pressure pulsation intensity of Plane 2 for condition 1.33 α_{ref}-1.18H_M. w_1 is the total function weight factor for efficiency, w_1=0.4, and w_2 is the total function weight factor for pressure pulsation, w_2=0.6. η represents the efficiency, $0 < \eta < 1$; C_p represents the pressure pulsation intensity, $0 < C_p < 0.2$. To avoid an excessive pressure pulsation intensity, which could lead to extreme and unreasonable objective functions, we have normalized C_p. This ensures that the objective function can properly reflect the performance of the turbine. The larger the value of G, the better the performance of the turbine is perceived, indicating a more stable and safer operation of the Francis turbine unit.

5.3 GA Setup and Optimization Strategy

A genetic algorithm is a search and optimization algorithm that retrieves high-quality individuals through a series of genetic operations such as crossover, variation, reproduction, and elimination. Regarding the settings of the genetic algorithm, this study adopts a crossover probability of 20%, a mutation probability of 5%, and a reproduction and elimination probability of 100% for the best and worst individuals. The specific genetic algorithm procedure is shown in Fig. 14. The crossover operation involves exchanging genetic information between two different individuals, while the mutation operation means that one or more genes of an individual undergo mutation,
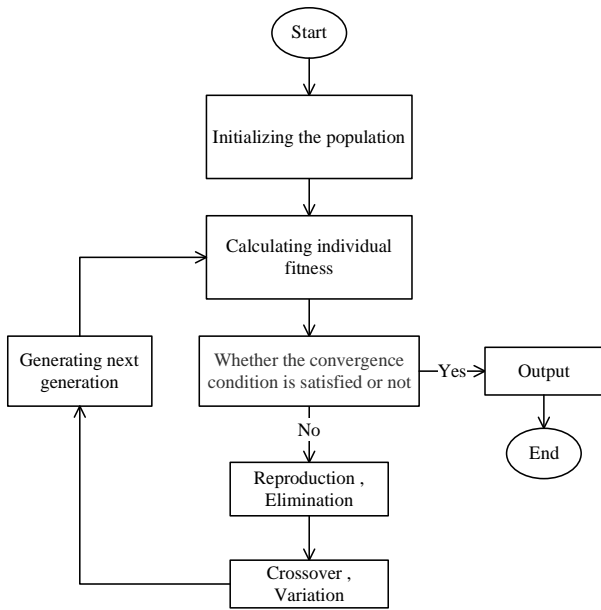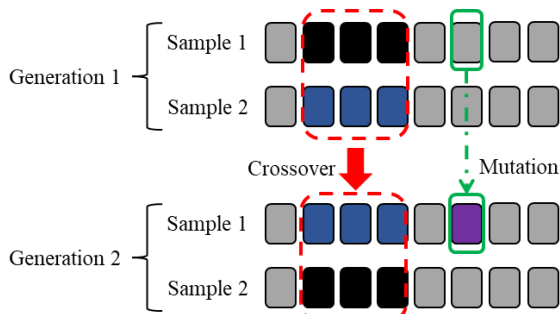
Fig. 14 Genetic algorithm flow chart

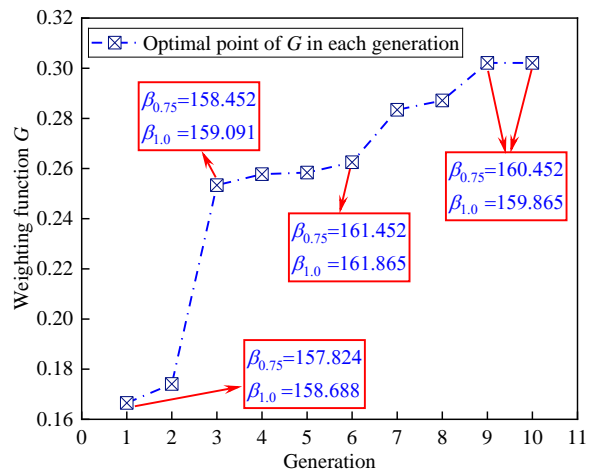**Fig. 15 Schematic diagram of crossover and variation gene manipulation**

Fig. 16 Iterative optimization process of the objective weighting function
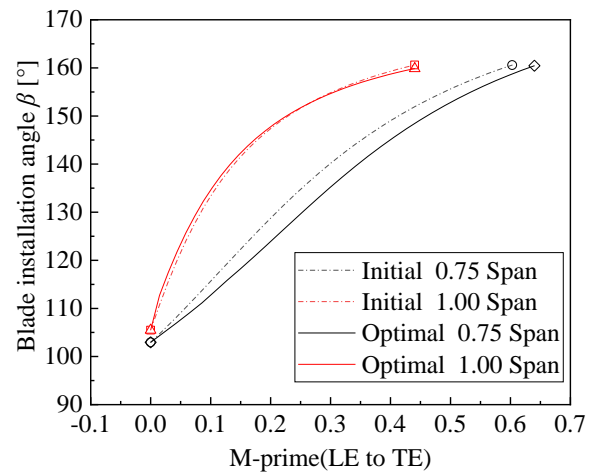
Fig. 17 Comparison of blade control curves for the initial and optimal schemes

thus altering the parameter information carried by the individual. Reproduction and elimination represent comparisons among all individuals in a generation, where the best individuals replace the worst ones, removing inferior genes from the population and retaining high-quality genes with desirable traits. A schematic diagram of the genetic operations of crossover and mutation is shown in Fig. 15.

5.4 Iterative Process of Optimization

Figure 16 shows the iterative optimization process of the genetic algorithm. As can be seen from the figure, after the eighth generation, the value of the weight function G in the ninth and tenth generations is kept constant; the research considers this point at which the optimization process has converged, and the combination of runner blade parameters corresponding to the optimal DTPP and efficiency performance has been obtained. Figure 17 demonstrates the comparison of the blade geometry control curves of the initial and optimal schemes. Since this research uses the blade trailing edge points to control the curves, $\beta_{0.75}=160.59°$ and $\beta_{1.0}=160.60°$ are set before the initial scheme and are adjusted to $\beta_{0.75}=160.452°$ and $\beta_{1.0}=159.865°$ after optimization. It can be seen in Fig. 15 that there is a significant difference between the two-blade

control curves. The optimized objective function value G reaches 0.30212.

6. COMPARATIVE ANALYSIS

6.1 Pressure and Velocity Vector Analysis

In this section, this research analyzed the pressure and velocity vectors on two monitoring surfaces before and after optimization for two conditions. Firstly, Fig. 18 shows the pressure and velocity vectors under condition α_{ref}-H_M. As can be seen, a low pressure region exists in the lower left of Plane 1 of the initial scheme and the velocity is high in this region. In addition, the wall pressure is high and fast, and the velocity vectors show that the vortex rotates counterclockwise, which is more consistent with the pressure trend, and the core does not completely align with the low pressure region but is slightly deviated from the center of the low-pressure region. In Plane 2, the low-pressure region is present in the upper left, with a slight increase in wall pressure. The vortex core is also out of alignment with the center of the low-pressure region, but
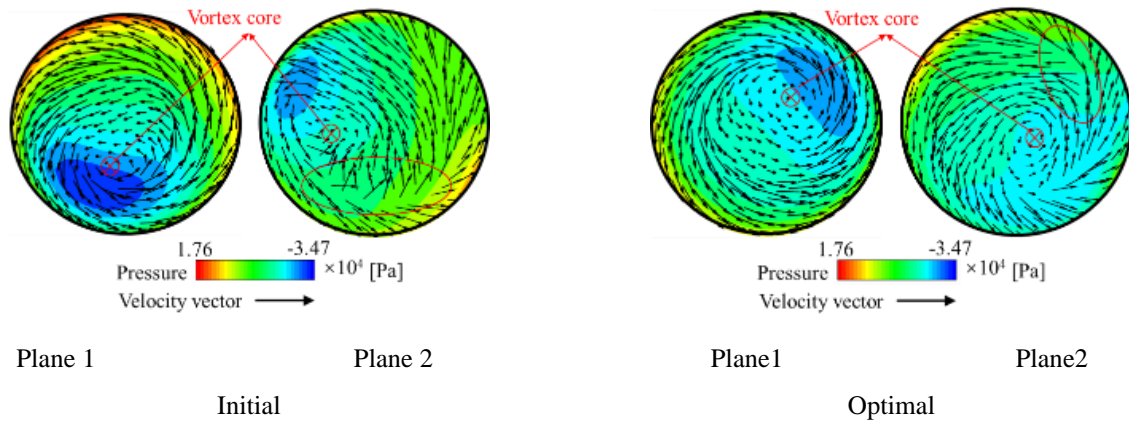
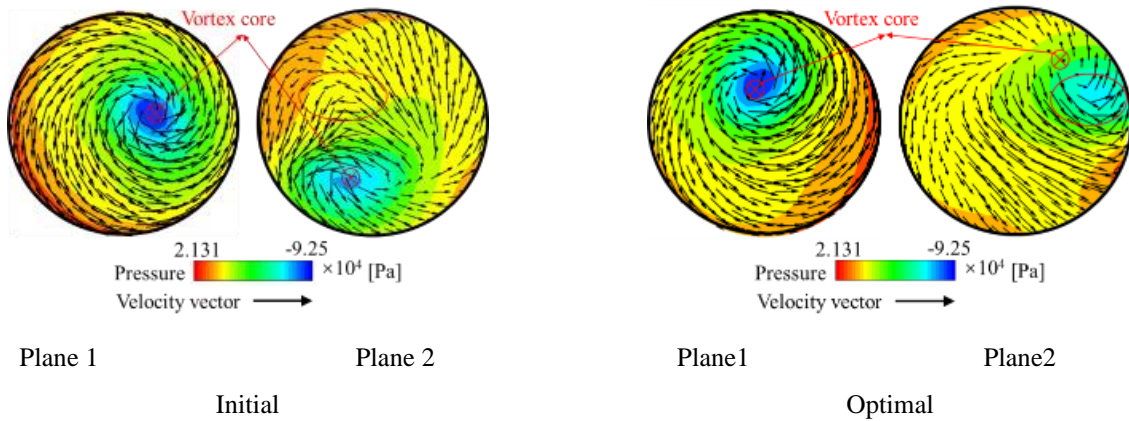**Fig. 18 Pressure and velocity vector diagram before and after optimization (condition α_{ref} -H_M)**

Fig. 19 Pressure and velocity vector diagram before and after optimization (condition 1.33 α_{ref}-1.18 H_M)

the direction of the velocity vector below the vortex core is chaotic, with a significant increase in velocity.

The low-pressure region in Plane 1 of the optimal scheme is slightly elevated compared to the initial scheme, but there is a significant decrease in the wall pressure values. In addition, the location of the optimized vortex core has also changed. The velocity vectors show that the vortex exists in the center and the vortex motion is more stable than before the optimization. The low-pressure region in Plane 2 is enlarged, there is an increase in the pressure values compared to the initial scheme, and the wall pressure values are generally high. The velocity vectors are more stable and orderly than before the optimization, there is a sudden change in the direction of the vortex around the wall, and the vortex core is present in the low-pressure region.

Figure 19 demonstrates the pressure and velocity vectors for condition 1.33 α_{ref}-1.18 H_M. The low-pressure region of the initial scenario in Plane 1 exists near the center region and increases towards the periphery, with the greatest pressure occurring at the lower left wall. From the point of view of velocity vectors, the vortex exists in the central region, the vortex core is in the same position as the center of the low-pressure region, and the pressure intensity matches the trend of the velocity vectors. The low-pressure region in Plane 2 is located in the lower left, and the pressure intensity is enhanced along the

counterclockwise rotation of the vortex, and the center of the vortex core is basically in the same position as the center of the low-pressure region. In addition, there is a sudden change in the vortex's direction, with a corresponding increase in the velocity.

The low-pressure region in Plane 1 of the optimal scheme is located above the center of the monitoring surface. Along the direction of the vortex's movement, the pressure intensity also shows an increasing trend, and the vortex core and the center of the low-pressure region are in the same position. Compared with the initial scheme, the pressure intensity is not significantly weakened, and the vortex speed and state are not significantly changed, but the vortex core position is changed with the vortex motion. Plane 2's low-pressure region exists in the upper right, and the pressure intensity of the peripheral wall is strong, but it is significantly reduced compared with the initial scheme. The vortex core and the center of the low-pressure region are not in the same location. From the point of view of the velocity vector, the optimized vortex motion is better, but there is slight turbulence in the velocity around the low-pressure region.

6.2 Details of PTN Method: Main Frequency, Amplitude, and Phase

This research performed a fast Fourier variation of the pressure pulsation signal based on the PTN method, and obtained the main frequency, amplitude, and phase cloud
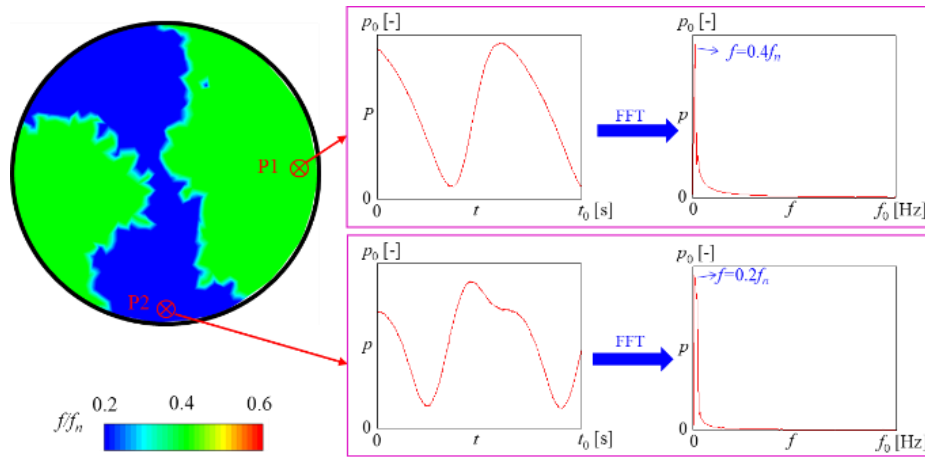
Fig. 20 Monitoring surface pressure pulsation and main frequency in Plane 1 (condition initial 1.33 α_{ref}-1.18 H_M)
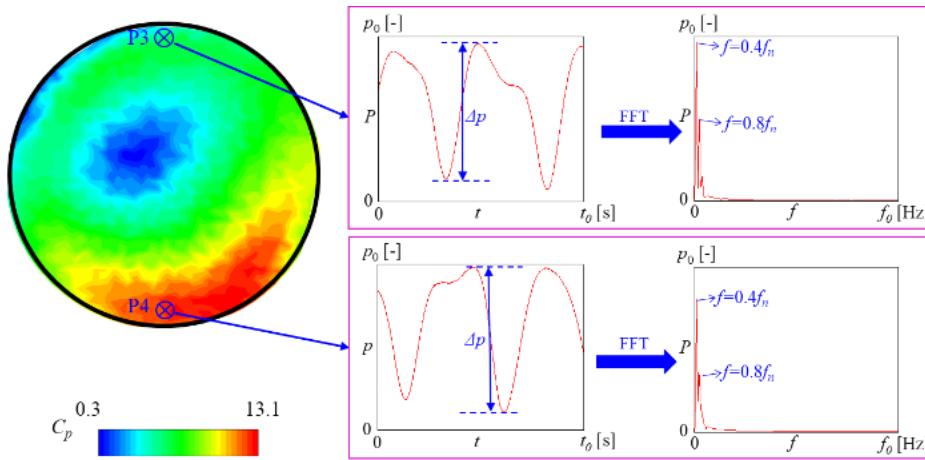

Fig. 21 Monitoring surface pressure pulsation and amplitude in Plane 1 (initial condition α_{ref} -H_M, f=0.4 f_n)

figures for the turbine, which are shown in Fig. 18, 19, and 20, respectively. In this research, the amplitude and the pressure pulsation amplitude p_0 were quantized to be dimensionless, see Eq. (15):

$$p_0 = \frac{p}{\rho g H} \tag{15}$$

Figure 20 shows the dominant frequency cloud of the pressure pulsation signal of the draft tube of the Francis turbine at Plane 1. This research establishes two monitoring points, P1 and P2, on Plane 1 for analysis. This research analyzes the pressure pulsation signal at point P1 and obtains the frequency domain figure, which shows that the dominant frequency of pressure pulsation is 0.4 f_n. Similarly, this research analyzes the pressure pulsation signal at point P2, which shows that the dominant frequency of pressure pulsation is 0.2 f_n, which corresponds to the dominant frequency cloud figure. In this way, all the monitoring points on Plane 1 are analyzed to obtain the dominant frequency of all the monitoring points. Then, the coordinates of the monitoring points and the dominant frequency data of each point are processed to obtain the dominant frequency cloud figure.

Figure 21 shows the DTPP intensity cloud figure in Plane 1. Two additional monitoring points, P3 and P4, were selected for analysis and to process the pulsation amplitude in the time-domain figure. Eq. (2) was used to

obtain the C_p value of the monitoring point via dimensionless quantification, where Δp is the peak-to-peak value of the pulsation amplitude. Moreover, this research performed a fast Fourier variation of the pulsation signal to obtain a frequency domain figure, and it was found that the pressure pulsations at points P3 and P4 were dominated by 0.4 f_n and 0.8 f_n. Therefore, following this procedure, the pulsation intensity cloud figure of Plane 1 was obtained, from which it can be seen that the pulsation intensity is larger at the edge of the lower wall and smaller in the middle. This research can assess then the motion pattern of the pulsation vortex accordingly in order to optimize and adjust the outlet angle of the runner blades.

Figure 22 shows the phase variation in DTPP in Plane 1. Again, two monitoring points, P5 and P6, are selected for phase variation analysis, and the time-domain figures show the phase variation in the pulsation signals, where $\Delta \varphi$ is the phase variation of the pulsation amplitude. From the frequency-domain figures, it can be seen that the DTPP at these two points are dominated by 0.4 f_n. Following this method, the obtained cloud figure shows that the pulsation signal at Plane 1 shows a tendency to change in the circumferential direction, and it is deduced that this pulsation trend is due to the formation of vortex bands in the draft tube. Therefore, this cloud figure shows the attenuation trend of the pulsation signal to some extent.
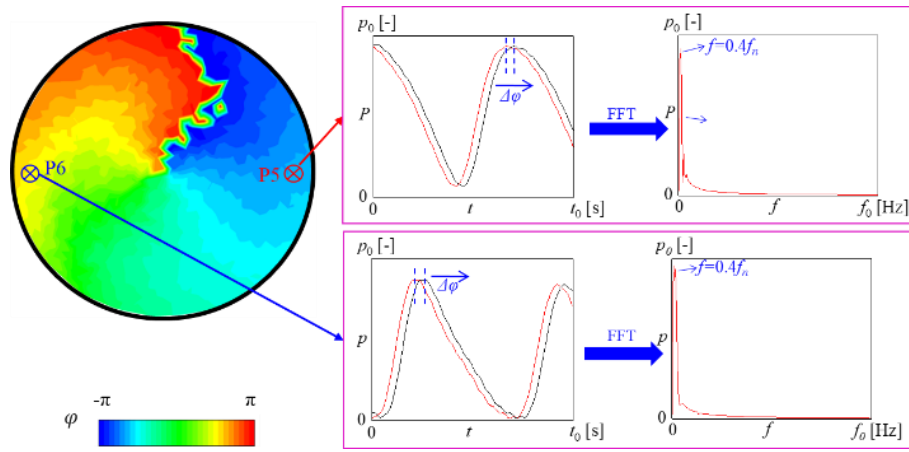
Fig. 22 Monitoring surface pressure and pulsation phase in Plane 1 (optimal condition 1.33 α_{ref}-1.18H_M, f=0.4f_n)
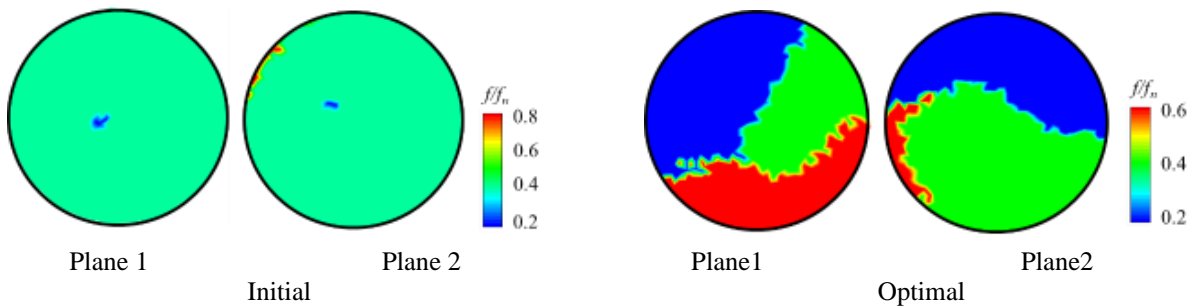

Fig. 23 Main frequency of initial and optimal schemes (condition α_{ref}-H_M)
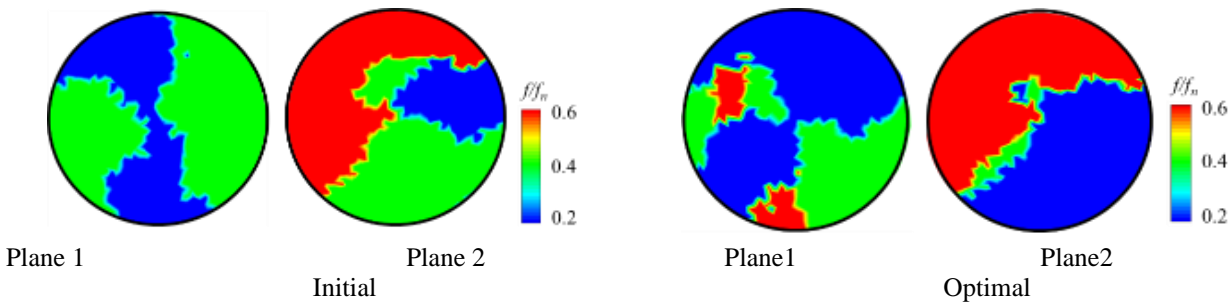

Fig. 24 Main frequency of initial and optimal schemes (condition 1.33 α_{ref}-1.18 H_M)

6.3 Main Frequency

In this section, this research analyzed the dominant frequencies of the pressure pulsation signals in Plane 1 and Plane 2 for condition α_{ref}-H_M in both the optimal and the initial schemes. Figure 23 presents the dominant frequencies of the pressure pulsation signals in both monitoring planes in the initial scheme. It shows that the dominant frequency is mainly at 0.4 f_n, accompanied by localized components at 0.2 f_n and 0.8 f_n. For the optimal scheme, in Plane 1, the dominant frequency of the pressure pulsation signals is mainly at 0.2 f_n, with additional components at 0.4 f_n and 0.6 f_n. In Plane 2, the dominant frequency of the pulsation signals is mainly at 0.4 f_n, but with some components at 0.2 f_n and a slight 0.6 f_n frequency component.

Figure 24 displays the dominant frequencies of the pressure pulsation signals in Plane 1 for the initial scheme under condition 1.33 α_{ref}-1.18 H_M. The dominant

frequency is found to be at 0.4 f_n. After optimization, there is an increase in localized dominant frequencies at 0.2 f_n and 0.6 f_n. In Plane 2, for the initial scheme, the dominant frequency is mainly at 0.4 f_n, with a localized dominant frequency at 0.2 f_n. After optimization, the dominant frequency at 0.4 f_n decreases, accompanied by an increase in the frequencies at 0.2 f_n and 0.6 f_n.

6.4 Amplitude of Typical Frequencies

Figure 25 illustrates a comparison of the pressure pulsation intensity between the initial and optimal schemes under condition α_{ref}-H_M with a frequency of 0.2 f_n. In the initial scheme, there is a noticeable region of high C_p near the left wall in Plane 1, forming a ring-shaped impact on the wall. In Plane 2, there are small spiral regions with high C_p in the top left and bottom right, along with a band-like low C_p region in the center. Comparing the optimal scheme with the initial scheme in Plane 1 and Plane 2, there is a significant decrease in C_p
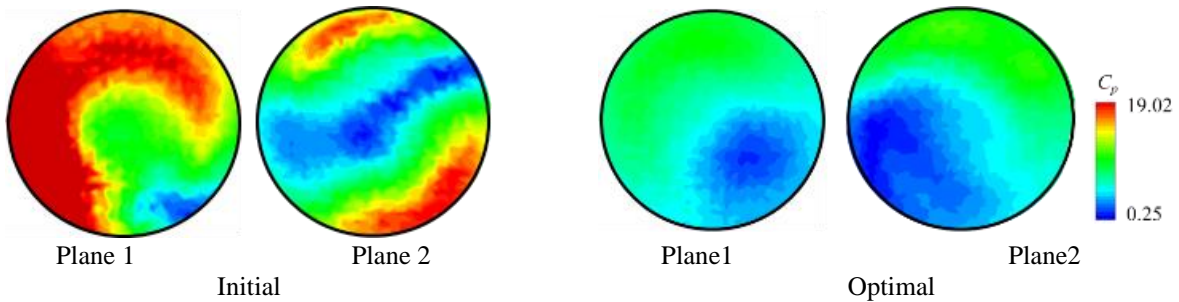
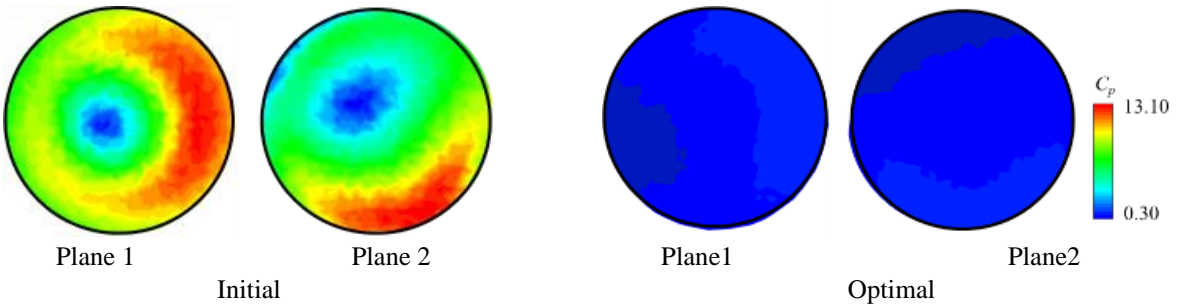Fig. 25 Pressure pulsation amplitude of initial and optimal schemes (condition α_{ref}-H_M, f=0.2 f_n)

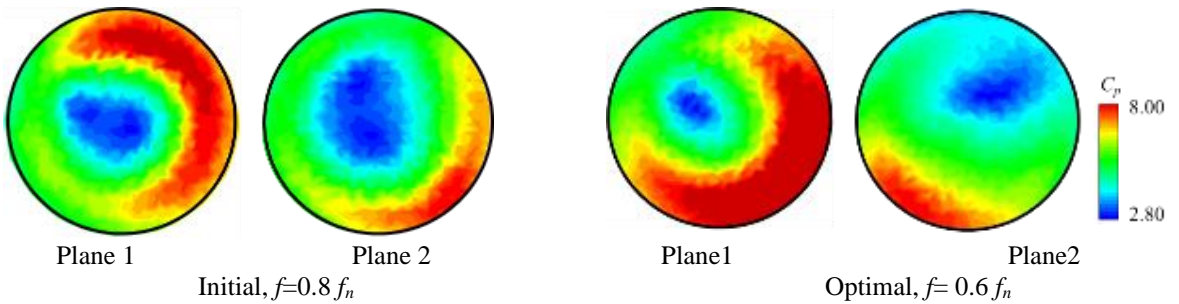Fig. 26 Pressure pulsation amplitude of initial and optimized schemes (condition α_{ref}-H_M, f=0.4 f_n)

Fig. 27 Pressure pulsation amplitude of initial and optimized schemes (condition α_{ref}-H_M, f=0.8 f_n, f=0.6 f_n)

of approximately 300%. Some of the regions with a high C_p in the initial scheme have disappeared, and the overall vortex intensity has decreased. The optimization has yielded clear improvements in reducing the pressure pulsation intensity.

Figure 26 presents a comparison of the C_p value between the initial and optimized schemes under condition α_{ref}-H_M with a frequency of 0.4 f_n. Comparing the C_p values of the optimal scheme with the initial scheme in both Plane 1 and Plane 2, there is a clear reduction in C_p. The high-C_p regions in the initial scheme have their C_p values reduced to around 0.3 in the optimized scheme. The optimization effect is very significant, resulting in a lower C_p in the draft tube, which is beneficial for the safe and stable operation of the turbine unit.

Figure 27 demonstrates a schematic representation of the pressure fluctuation intensities between the initial and optimal schemes under condition α_{ref}-H_M at frequencies of 0.8 f_n and 0.6 f_n. In the initial scheme, the dominant frequency of the pressure pulsation at 0.8 f_n disappears after optimization, and a new dominant frequency at 0.6 f_n emerges. At the frequency of 0.8 f_n in the initial scheme, strong C_p regions appear on the wall side in both Plane 1 and Plane 2. Additionally, the C_p value in Plane 1 is

significantly higher than in Plane 2 by approximately 200%. Both monitoring planes exhibit low-C_p regions at the center, which might be related to the form of the vortex ropes in the draft tube, resulting in a pressure pulsation impact on the wall. At the frequency of 0.6 f_n, the strong-C_p regions still exist in an arc shape on the wall, but in Plane 1, the C_p value reaches around 13, covering a larger area and resulting in stronger impact on the wall. In Plane 2, the C_p value is lower at around 7.5 on the wall side, indicating a relatively moderate impact on the wall, but it still cannot be overlooked.

Figure 28 illustrates a comparison of the pressure pulsation intensities between the initial and optimized schemes under condition 1.33 α_{ref}-1.18 H_M at a frequency of 0.2 f_n. In Plane 1, the optimized scheme exhibits a noticeable expansion of the ring-shaped region of high C_p value compared to the initial scheme, approximately 10% larger. However, since there is no impact on the wall of the draft tube at the center of the monitoring plane, this pulsation is considered to be relatively safe. In Plane 2, the optimal scheme shows a significant enhancement and expansion of the arc-shaped region with high-pressure pulsation in the bottom right, approximately 15% larger than in the initial scheme. Moreover, this region is close
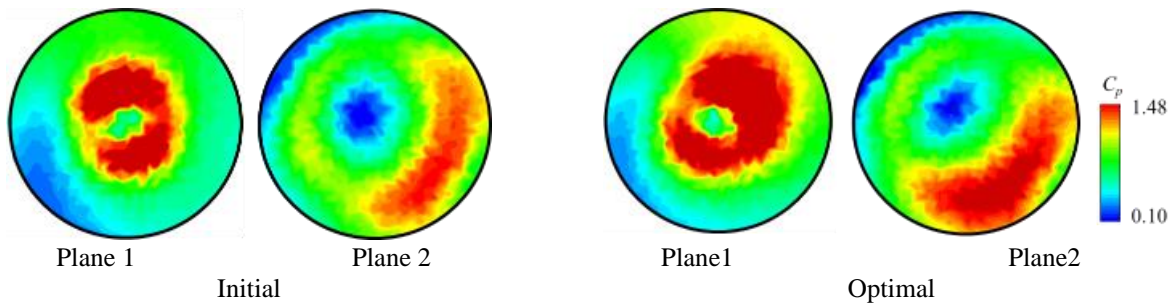
Plane 1 Plane 2 Plane1 Plane2

Initial Optimal

Fig. 28 Pressure pulsation amplitude of initial and optimal schemes (condition 1.33 α_{ref}-1.18 H_M, f=0.2 f_n)
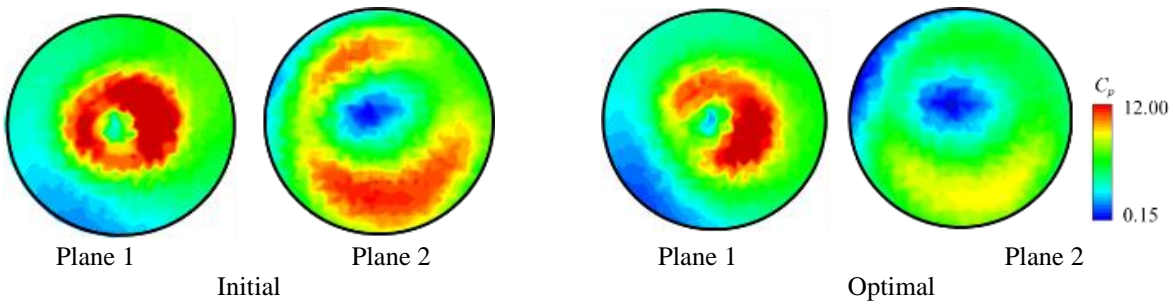

Plane 1 Plane 2 Plane 1 Plane 2

Initial Optimal

Fig. 29 Pressure pulsation amplitude of initial and optimal schemes (condition 1.33 α_{ref}-1.18 H_M, f=0.4 f_n)

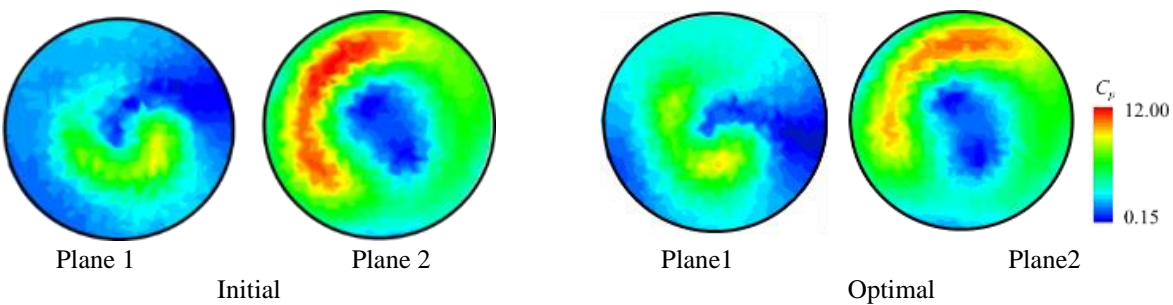Plane 1 Plane 2 Plane1 Plane2

Initial Optimal

Fig. 30 Pressure pulsation amplitude of initial and optimal schemes (condition 1.33 α_{ref}-1.18 H_M, f=0.6 f_n)

to the wall of the draft tube, indicating that the pulsation may have a certain impact on the wall.

Figure 29 shows a comparison of the pressure pulsation intensities between the initial and optimal schemes under condition 1.33 α_{ref}-1.18 H_M at a frequency of 0.4 f_n. In Plane 1, the ring-shaped region of strong C_p values in the initial scheme shows a reduction of approximately 25% after optimization. The optimal scheme in Plane 1 shows an improved pulsation situation, where the strong-C_p region is closer to the center of the draft tube, resulting in a smaller impact on the wall pulsation. In Plane 2, the double arc-shaped regions of high C_p values in the initial scheme have significantly weakened after optimization, with a reduction in intensity of approximately 60%. The C_p value in this monitoring plane decreases more prominently, leading to a reduction in the impact of wall pulsation.

Figure 30 presents a comparison of C_p values between the initial and optimal schemes under condition 1.33 α_{ref}-1.18 H_M at a frequency of 0.6 f_n. In Plane 1, the optimal scheme shows a localized increase in pressure pulsation compared to the initial scheme, approximately 20% higher. However, the overall intensity of the pressure pulsation is not high. In Plane 2 of the optimal scheme,

there is a slight decrease in the arc-shaped region of high C_p values compared to the initial scheme, approximately 5% lower. This pulsation impact region is still at a certain distance from the wall of the draft tube, resulting in a relatively weaker influence on the draft tube.

6.5 Phase and Phase Difference

Figure 31 illustrates the phase variation in pressure pulsation signals between the initial and optimal schemes under condition α_{ref}-H_M at a frequency of 0.2 f_n. In the initial scheme, the phase variation can be observed from Plane 1 to Plane 2, showing a clockwise phase change. The phase variation in the monitoring surface of Plane 1 remains within one cycle, while in Plane 2, the phase change spans one cycle. In the optimal scheme, the phase of the pressure pulsation signals in both Plane 1 and Plane 2 decay within one cycle. From the phase diagrams of the two surfaces, it can be seen that the phase change of the optimal pulsation signals still follows a clockwise trend.

Figure 32 shows the phase variation in pressure pulsation signals between the initial and optimal schemes under condition α_{ref}-H_M at a frequency of 0.4 f_n. In the initial scheme, the pressure pulsation signals on both monitoring surfaces, Plane 1 and Plane 2, span one cycle,
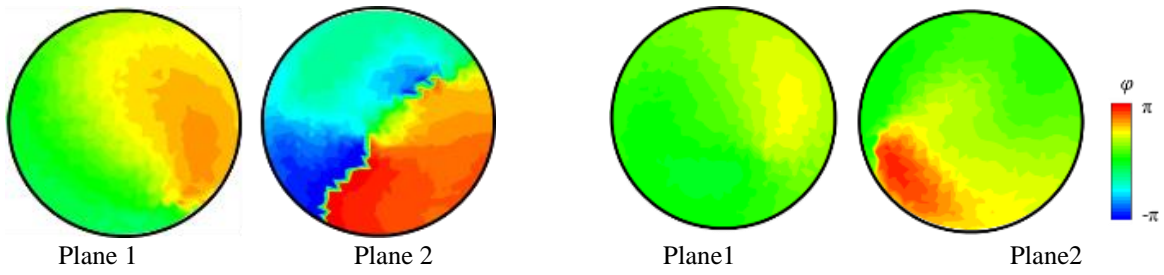
Fig. 31 Phases of initial and optimal schemes (condition α_{ref}-H_M, f=0.2 f_n)
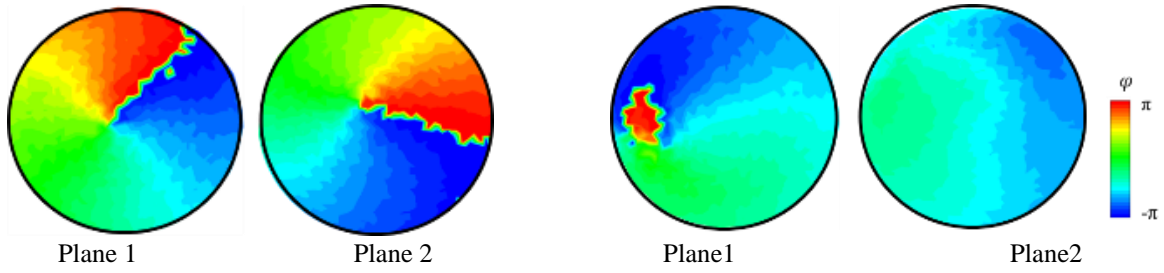

Fig. 32 Phases of initial and optimal schemes (condition α_{ref}-H_M, f=0.4 f_n)
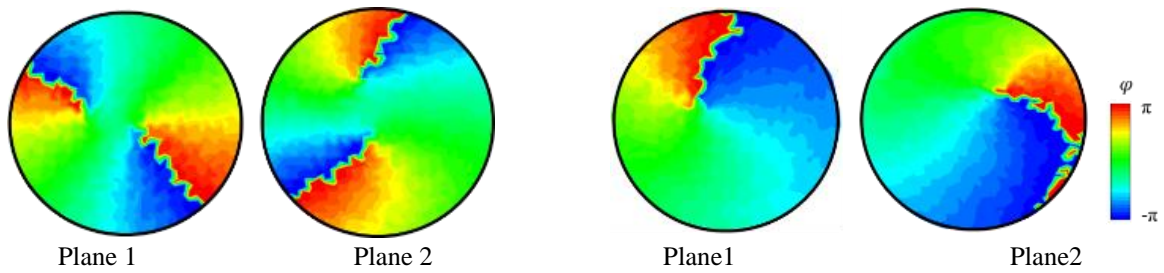

Fig. 33 Phases of initial and optimal schemes (condition α_{ref}-H_M, f=0.8 f_n , f=0.6 f_n)
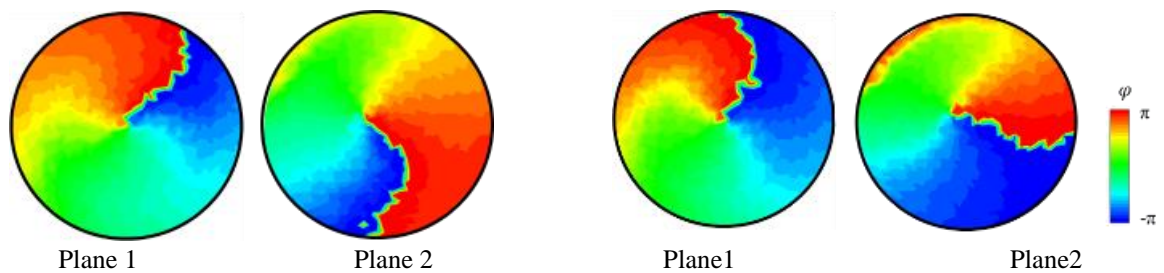

Fig. 34 Phases of initial and optimal schemes (condition 1.33 α_{ref}-1.18 H_M, f=0.2 f_n)

with a clockwise attenuation trend. In the optimal scheme, in Plane 1, there is a localized phase variation spanning one cycle for the pulsation signals, while most of the region shows attenuation within one cycle. In Plane 2, the overall region exhibits attenuation within one cycle, still following a clockwise direction.

Figure 33 presents the phase variation in pressure pulsation signals between the initial and optimal schemes under condition α_{ref}-H_M at frequencies of 0.8 f_n and 0.6 f_n. In the initial scheme, the dominant frequency of the pressure pulsation is at 0.8fn. Both monitoring surfaces, Plane 1 and Plane 2, exhibit two cycles of attenuation for

the pulsation signals. This indicates that the pressure pulsation signals at this dominant frequency span two cycles during attenuation. In the optimal scheme, the dominant frequency of the pressure pulsation is at 0.6 f_n. The pulsation signals attenuate within one cycle. Hence, it can be observed that the phase attenuation period of the pulsation signals differs for different frequencies.

Figure 34 shows the phase change in the pressure pulsation signals of the initial and optimal schemes under condition 1.33 α_{ref}-1.18 H_M, f=0.2 f_n. For the initial scheme, the phase of the pulsation signals from the monitoring surface of Plane 1 to Plane 2 shows a
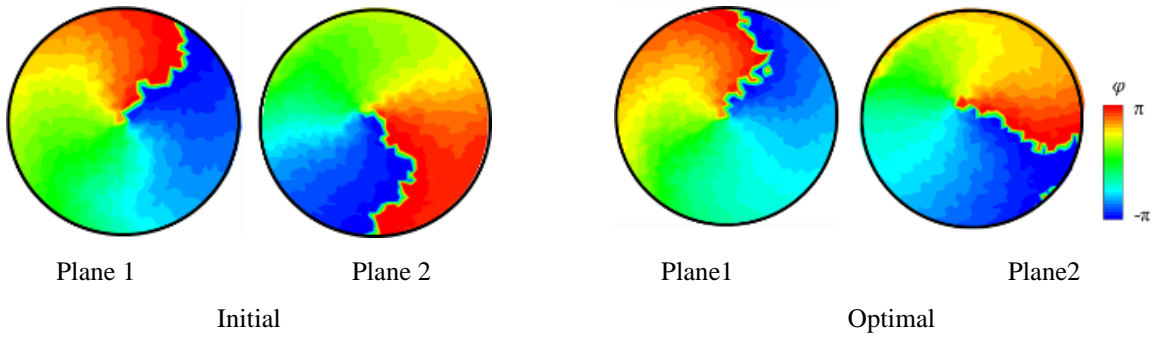
Plane 1   Plane 2   Plane1   Plane2

Initial   Optimal

Fig. 35 Phases of initial and optimal schemes (condition 1.33 α_{ref}-1.18 H_M, f=0.4 f_n)

Plane 1   Plane 2   Plane1   Plane2
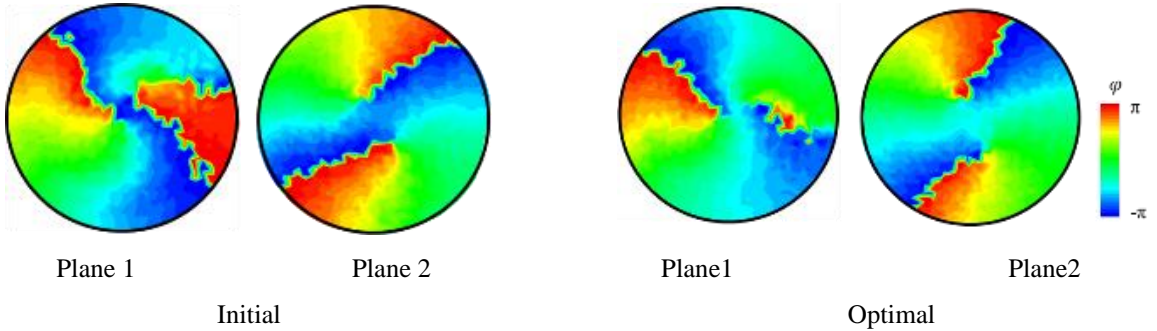
Initial   Optimal

Fig. 36 Phases of initial and optimal schemes (condition 1.33 α_{ref}-1.18 H_M, f=0.6 f_n)
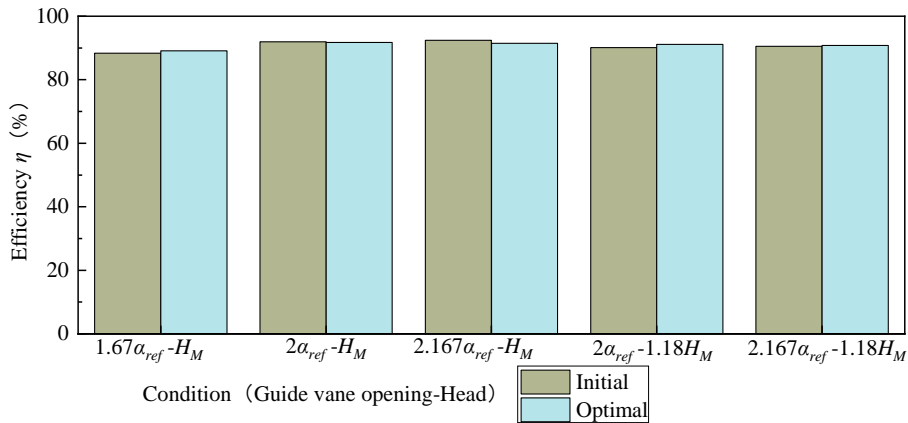

Fig. 37 The efficiency of the initial and optimal schemes

clockwise trend of decaying, and both exceed one cycle. In the optimized scenario, the pulsation signals are the same as the original scenario, and the time point of completing one cycle has been advanced.

Figure 35 shows the phase change in the pressure pulsation signals of the initial and optimal schemes under condition 1.33 α_{ref}-1.18 H_M, f=0.4 f_n. Both the original and optimal schemes have pressure pulsation signals that decay across one cycle and clockwise decay signals, with the optimal scheme having an earlier decay time point across the cycle than the initial scheme.

Figure 36 shows a schematic diagram of the phase change in the pressure pulsation signal for the initial and optimal schemes for condition 1.33 α_{ref}-1.18 H_M, f=0.6 f_n. In the initial scheme, there are two decaying trends in the two monitoring surfaces, indicating that the pulsation

signal at this frequency moves across two cycles in a decaying motion with a clockwise direction. While there is one obvious trend of decay across one cycle and one local trend of decay across one cycle on the monitoring surface of Plane 1 in the optimal scheme, there are two obvious pulsation signal decay trends across two cycles in Plane 2. It is speculated that the local pulsation decay trend in Plane 1 is enhanced when it reaches the monitoring surface in Plane 2.

6.6 Efficiency

In this section, the change in efficiency of the Francis turbine unit between the initial and the optimal scheme is compared. It can be seen from Fig. 37 that the efficiency of the turbine is lower in the optimal scheme than in the initial scheme in condition 2 α_{ref}-H_M and condition 2.167 α_{ref}-H_M, but in other conditions, there is a slight increase

in efficiency compared to the initial scheme. This is in line with our original optimization objective, that is, to ensure or improve the unit's efficiency as much as possible based on reducing the pressure pulsation in the draft tube. Therefore, this optimization meets the corresponding requirements.

7. CONCLUSIONS

This study uses a genetic algorithm and the pulsation tracking network method to optimize the design of the draft tube pressure pulsation in Francis turbines. Numerical tracking and visual analysis were conducted on the dominant frequency of the draft tube pressure pulsation, as well as the propagation and attenuation of pulsation signals. The experimental results verified the reliability of the numerical simulations. Therefore, this study concludes with the following three points:

1. This article utilizes the PTN (pulsation tracking network) method to analyze the draft tube pressure pulsation in Francis turbines. It is shown that the deviation of Francis turbines from the optimal operating conditions is the fundamental reason for the generation of pressure pulsations. The circumferential velocity component at the turbine outlet is the decisive factor in causing pressure pulsation. When the circumferential velocity component interacts with the axial velocity component, it forms a helical vortex, resulting in vortex-induced pressure pulsation, which is the main type of pressure pulsation observed in this study. The visualization of tailwater pipe pressure pulsation influenced by helical vortices is an advantage of the PTN method. For example, the arced shape of the strong-C_p region in the initial design, as shown in Fig. 25, is validated, which aligns with the motion state of helical vortices.

2. In this study, the draft tube pressure pulsation was optimized, ensuring or improving efficiency. The genetic algorithm was used to optimize the placement angle of the turbine blade outlet, resulting in an optimal turbine configuration that satisfied the weight objective function. For the initial turbine design, the efficiency was 91.48% in condition 2 α_{ref}-H_M and 83.04% in condition 1.33 α_{ref}-1.18 H_M, with a weight value G of 0.167. For the optimal turbine design, the efficiency was 91.75% in condition 2 α_{ref}-H_M and 86.52% in Condition 1.33 α_{ref}-1.18 H_M, with a weight value G of 0.302. The efficiency improved by 0.27% and 3.48% for the two operating conditions, respectively. There was an overall improvement in the turbine's performance, with the weight function increasing by 0.135 and an obvious reduction in pressure pulsation.

3. In this study, this research analyzed the pressure pulsation of the initial and optimal schemes using the PTN method, focusing on three aspects: dominant pulsation frequencies, pulsation intensity at typical frequencies, and phase differences. First, when the turbine operated under off-design conditions α_{ref}-H_M and 1.33 α_{ref}-1.18 H_M, this research identified dominant frequencies for DTPP at 0.2, 0.4, 0.6, and 0.8 f_n. The initial scheme had a dominant frequency of 0.4 f_n for pulsation, while the optimal scheme had a dominant frequency of 0.2 f_n in Plane 1 and a dominant frequency of 0.4 f_n in Plane 2. Next, this research analyzed the C_p value at typical frequencies and found that the pulsation intensity decreased by 300% under condition α_{ref}-H_M, f=0.2 f_n. Under condition α_{ref}-H_M, f=0.4 f_n, the pulsation intensity decreased to 0.3. Under condition 1.33 α_{ref}-1.18 H_M, f=0.2 f_n, the strong-C_p region in Plane 1 increased by approximately 10% compared to the initial design. For Plane 2, the optimal design showed an approximately 15% increase in the strong-C_p region in the lower right arc compared to the initial design. In Condition 1.33 α_{ref}-1.18 H_M, f=0.4 f_n, the pulsation intensity decreased by approximately 25% and 60% at the two monitoring surfaces, respectively. Finally, this research analyzed the phase variations and revealed the different attenuation directions and periods of pressure pulsation on the circumferential interface.

In general, this study provides a visualization of pressure pulsation in Francis turbine draft tubes and optimizes it using algorithms. The findings will help enhance operational stability and security of hydropower turbines, and the methodology can be applied in similar engineering cases.

ACKNOWLEDGEMENT

CONFLICT OF INTEREST

The authors have no conflicts to disclose.

AUTHORS CONTRIBUTION

Jiahao Lu: Conceptualization, Methodology, Writing—original draft; **Ran Tao:** Investigation, Data curation, Writing—review and editing.

REFERENCES

Abu Shahzer, M., Cho, Y., & Kim, J. H. (2023) Investigation of cavitating vortex rope instabilities and its suppression inside a Francis turbine model with Thoma number variation. *Physics of Fluids*, *35*(2), 033310. https://doi.org/10.1063/5.0140973

Amooghin, A. E., Jafari, S., Sanaeepur, H., & Kargari, A. (2015). Computational fluid dynamics simulation of bubble coalescence and breakup in an internal airlift reactor: Analysis of effects of a draft tube on hydrodynamics and mass transfer. *Applied Mathematical Modelling*, *39*(5-6), 1616-1642. https://doi.org/10.1016/j.apm.2014.09.020

Bosioc, A. I., Susan-Resiga, R., & Tanasa, C. (2012) Unsteady pressure analysis of a swirling flow with vortex rope and axial water injection in a discharge cone. *Journal of Fluids Engineering-Transactions of the ASME*, *134*(8), 081104. https://doi.org/10.1115/1.4007074

Celik, I. B., Ghia, U., Roache, P. J., & Freitas, C. J. (2008).

Procedure for estimation and reporting of uncertainty due to discretization in CFD applications. *Journal of Fluids Engineering*, *130*, 78001. https://doi.org/10.1115/1.2960953

Chen, H., Zhou, D., & Zheng, Y. (2019). Influence of impeller regulation on transient characteristics of Kaplan turbine during load rejection process. *Journal of Huazhong University of Science and Technology. Nature Science*, *47*(8), 114-119. https://doi.org/10.13245/j.hust.190822

Chirkov, D. V., Shcherbakov, P. K., & Turuk, P. A. (2018). Numerical investigation of the air injection effect on the cavitating flow in Francis hydro turbine. *Thermophysics and Aeromechanics*, *24*(5), 691-703. https://doi.org/10.1134/S0869864317050055

Ge, J., Qiu, Y., Wu, C., & Pu, G. (2008). Summary of genetic algorithms research. *Application Research of Computers*, *25*(10), 2911-2916. https://doi.org/10.3969/j.issn.1001-3695.2008.10.008

Graham, J. T., Rollett, A. D., & LeSar, R. (2016). Fast Fourier transform discrete dislocation dynamics. *Modelling and Simulation in Materials Science and Engineering*, *24*(8), 085005. https://doi.org/10.1088/0965-0393/24/8/085005

International Electrotechnical Commission (IEC). (1999). Hydraulic turbines, storage pumps and pump turbines-model acceptance tests. *International Standard IEC* 60193.

Jin, F., Li, P., Tao, R., Xiao, R. F., & Zhu, D. (2023). Study of vortex rope for the flow field pulsation law. *Ocean Engineering*, *273*, 114026. https://doi.org/10.1016/j.oceaneng.2023.114026

Jin, F., Tao, R., & Xiao, R. F. (2021). A spatially distributed network for tracking the pulsation signal of flow field based on CFD simulation: method and a case study. *Fractal and Fractional*, *5*(4), 181. https://doi.org/10.3390/fractalfract5040181

Joy, J., Raisee, M., & Cervantes, M. J. (2022). Hydraulic performance of a francis turbine with a variable draft tube guide vane system to mitigate pressure pulsations. *Energies*. *15*(18), 6542. https://doi.org/10.3390/en15186542

Kan, K., Xu, Y. H., & Shen, L. (2023a). Numerical study of instability mechanism in the air-core vortex formation process. *Engineering Applications of Computational Fluid Mechanics*, *17*(1), 2156926. https://doi.org/10.1080/19942060.2022.2156926

Kan, K., Xu, Y. H., & Yang, Z. X. (2023b). Vortex-induced energy loss of a mixed-flow waterjet pump under different operating conditions. *Acta Mechanica Sinica*, *39*(9), 323064. https://doi.org/10.1007/s10409-023-23064-x

Kekes, S. (2011). Fossil energy sources, climate change, and alternative solutions. *Energy Sources Part A-Recovery Utilization and Environmental Effects*, *33*(12), 1184-1195.

https://doi.org/10.1080/15567030903330660

Kumar, S., Cervantes, M. J., & Gandhi, B. K. (2021). Rotating vortex rope formation and mitigation in draft tube of hydro turbines–A review from experimental perspective. *Renewable and Sustainable Energy Reviews*, *136*, 110354. https://doi.org/10.1016/j.rser.2020.110354

Li, D. Y., Ren, Z. P., & Wang, H. J. (2021a). Spatio-temporal evolution mechanism of cavitation vortex ropes in a swirling flow. *Physics of Fluids*, *33*(10), 104107. https://doi.org/10.1063/5.0067735

Li, D., Yu, L., & Wei, X. Z. (2021b). Runner cone optimization to reduce vortex rope-induced pressure fluctuations in a Francis turbine. *Science China-Technological Sciences*, *64*(9), 1953-1970. https://doi.org/10.1007/s11431-021-1867-2

Lu, J. H., Zhang, F. F., Tao, R., Li, X. Q., Zhu D., & Xiao R. F. (2023). Optimization of runner and vane blade angle of an oscillating water column based on genetic algorithm and neural network. *Ocean Engineering*, *248*, 115257. https://doi.org/10.1016/j.oceaneng.2023.115257

Lu, Z. H., Tao, R., Jin, F. Y., Li, P. X., Xiao, R. F., & Liu, W. C. (2021). The temporal-spatial features of pressure pulsation in the diffusers of a large-scale vaned-voluted centrifugal pump. *Machines*, *9*(11), 266. https://doi.org/10.3390/machines9110266

Luo, Z. M., Nie, C., & Gao, S. M. (2022). The effect of J-groove on vortex suppression and energy dissipation in a draft tube of francis turbine. *Energies*, *15*(5), 1707. https://doi.org/10.3390/en15051707

Mayer, A. (2022). Fossil fuel dependence and energy insecurity. *Energy Sustainability and Society*, *12*(1), 27. https://doi.org/10.1186/s13705-022-00353-5

Miao, S. C., Yang, J. H., Wang, X. H., Li, J. C., & Li, T. L. (2015). Blade pattern optimization of the hydraulic turbine based on neural network and genetic algorithm. *Journal of Aerospace Power*, *30*(8), 1918-1925. https://doi.org/10.13224/j.cnki.jasp.2015.08.015

Nasir, J., Javed, A., Ali, M., Ullah, K., & Abbas Kazmi, S. (2022). Capacity optimization of pumped storage hydropower and its impact on an integrated conventional hydropower plant operation. *Applied Energy*, *323*, 119561. https://doi.org/10.1016/j.apenergy.2022.119561

Sato, K., Tamura, Y., & Tani, K. (2014). Multi-objective optimization for francis turbine runner using genetic algorithm. *Proceedings of the Asme International Mechanical Engineering Congress and Exposition*, 7, V007T09A073. https://doi.org/10.1115/IMECE2014-36401

Tao, R., Xiao, R. F., Yang, W., Wang, F. J., & Liu, W. C. (2014). Optimization for cavitation inception performance of pump-turbine in pump mode based on genetic algorithm. *Mathematical Problems in Engineering*, *2014*, 234615.

https://doi.org/10.1155/2014/234615

Tao, R., Xiao, R. F., Zhu, D., & Wang, F. J. (2018). Multi-objective optimization of double suction centrifugal pump. *Proceedings of The Institution of Mechanical Engineers Part C-Journal of Mechanical Engineering Science*, *232*(6), 1108-1117. https://doi.org/10.1177/0954406217699020

Wang, Y., Shen, T. S., Tan, C. S., Fu, J., & Guo, S. R. (2021). Research status, critical technologies, and development trends of hydraulic pressure pulsation attenuator. *Chinese Journal of Mechanical Engineering*, *34*(1), 14. https://doi.org/10.1186/s10033-021-00532-z

Yang, F., Li, Z. B., Yuan, Y., Lin, Z. K., Zhou, G. X., & Ji, Q.W. (2022). Study on vortex flow and pressure fluctuation in dustpan-shaped conduit of a low head axial-flow pump as turbine. *Renewable Energy*, *196*, 856-869. https://doi.org/10.1016/j.renene.2022.07.024

Yu, A., Tang, Q., Wang, X., Zhou, D., &Liu, J. (2019). Investigation of the pressure fluctuation alleviation in a hydraulic turbine by runner modification. *Water*, *11*(7), 1332. https://doi.org/10.3390/w11071332

Yu, A., Wang, Y. S., Tang, Q. H., Lv, Q. H., & Yang, Z. P. (2021). Investigation of the vortex evolution and hydraulic excitation in a pump-turbine operating at different conditions. *Renewable Energy*, *171*, 462-478. https://doi.org/10.1016/j.renene.2021.02.131

Yu, A., Zou, Z. P., Zhou, D. Q., Zheng, Y., & Luo, X. W. (2020). Investigation of the correlation mechanism between cavitation rope behavior and pressure fluctuations in a hydraulic turbine. *Renewable Energy*, *147*, 1199-1208, Part 1. https://doi.org/10.1016/j.renene.2019.09.096

Zhang, Y., Binsted, M., Iyer, G., Kim, S., Wild, T., & Zhao, M. Q. (2022). Long-term basin-scale hydropower expansion under alternative scenarios in a global multisector model. *Environmental Research Letters*. *17*(11), 114029. https://doi.org/10.1088/1748-9326/ac9ac9

Zhao, R., Zhuge, W., Ma, X., et al. (2020). Impacts of pulse frequency and amplitude on the unsteady characteristics of a two-stage turbine. *Journal of Automotive Safety and Energy*, *11*(1), 127-134. https://doi.org/10.1016/j.energy.2018.01.125

Zheng, Y., Jiang, W., Chen, Y., & Sun A. (2018). Investigation on low frequency pulsating and draft tube vortex of tubular turbine. *Transactions of the Chinese Society for Agricultural Machinery*, *49*(4), 165-171. https://doi.org/10.6041/j.issn.1000-1298.2018.04.019

Zhou, X., Shi, C. Z., Miyagawa, K., & Wu, H. G. (2021). Effect of modified draft tube with inclined conical diffuser on flow instabilities in Francis turbine. *Renewable Energy*, *172*, 606-617. https://doi.org/10.1016/j.renene.2021.03.075